npj | Flexible Electronics

www.nature.com/npjflexelectron

ARTICLE OPEN

Check for updates

Sensorized tissue analogues enabled by a 3D-printed conductive organogel

Michael R. Crump[1]✉, Sophia L. Bidinger[1,2], Felippe J. Pavinatto[1], Alex T. Gong[2], Robert M. Sweet[2,3] and J. Devin MacKenzie[1,4]

State-of-the-art tissue analogues used in high-fidelity, hands-on medical simulation modules can deliver lifelike appearance and feel but lack the capability to provide quantified, real-time assessment of practitioner performance. The monolithic fabrication of hybrid printed/textile piezoresistive strain sensors in a realistic Y/V plasty suture training pad is demonstrated. A class of 3D-printable organogels comprised of inexpensive and nonhazardous feedstocks is used as the sensing medium, and conductive composite threads are used as the electrodes. These organogels are comprised of a glycol-based deep-eutectic solvent (DES) serving as the ionic conductor and 3-trimethoxysilylmethacrylate-capped fumed silica particles serving as the gelating agent. Rheology measurements reveal the influence of fumed silica particle capping group on the mixture rheology. Freestanding strain sensors demonstrate a maximum strain amplitude of 300%, negligible signal drift, a monotonic sensor response, a low degree of hysteresis, and excellent cyclic stability. The increased contact resistance of the conductive thread electrodes used in place of wire electrodes do not make a significant impact on sensor performance. This work showcases the potential of these organogels utilized in sensorized tissue analogues and freestanding strain sensors for widespread applications in medical simulation and education.

npj Flexible Electronics (2021)5:7 ; https://doi.org/10.1038/s41528-021-00104-0

INTRODUCTION

Since Safar, Lind, and Laerdal invented the first full-size medical simulator, *Resusci Anne*, in 1961[1], the healthcare simulation field has expanded tremendously as part of a larger effort to reduce medical error[2]. To date, there exist 174 healthcare simulation centers accredited by the Society for Simulation in Healthcare[3], and, as of 2019, there were 93 accredited by the American College of Surgeons Accredited Education Institutes[4]. Healthcare simulation has improved medical skill acquisition across a wide range of practitioner seniorities[5], and a recent meta-analysis by Beal et al.[6] indicated that high-fidelity simulations were more effective than low-fidelity simulations in improving medical performance-based outcomes. Lifelike optical and mechanical properties of artificial tissue combined with dynamic manikin actuation driven by realistic cardiovascular physiology models distinguish the former from the latter[6]. The next significant development in healthcare simulation is the integration of sensors into high-fidelity manikins to deliver more realistic patient-provider interactions and to generate data for objective performance assessments[7]. As many medical and surgical procedures involve the manipulation and deformation of tissue, a strain sensor monolithically integrated into artificial tissue models with a minimal footprint would quantify tissue deformation in a wide range of healthcare simulation modules without sacrificing fidelity. Reconstructive surgical skin procedures such as skin flaps especially would benefit from the quantification of strain as the degree of strain experienced by a healing dermal wound influences viability of the tissue and the extent of permanent scarring[8]. Most current training simulation models use sensor-free artificial skin or pig feet for surgical practice[9]. Optically marked tissue models have delivered objective assessment opportunities for reconstructive procedures like skin flaps[10]. We propose integrating sensorized tissue skin flap models for automated assessment.

A strain sensor is composed of a conductive channel with two electrodes connected to supporting readout electronics. Either changes in resistance (piezoresistive) or capacitance (piezocapacitive) can be measured in response to strain[11]. As detailed in our previous work[12], piezoresistive sensors are preferred for applications in medical simulation due to (1) their minimized footprint in tissue models, and (2) their insusceptibility to stray capacitive interference. Initial piezoresistive sensing channel mediums were composed of a network of solid conductors dispersed in an elastomeric matrix[11,13,14]. While these sensors possess high sensitivities, they suffer from significant signal drift, which arises from the permanent displacement of embedded conductors in response to applied strains[11,15,16]. A nonmonotonic response is observed in several recent publications[17–19], which introduces uncertainty to sensor readout interpretation and consequentially requires nontrivial signal processing.

In light of these inherent limitations of composite-based piezoresistive strain sensors, a burgeoning design strategy is to embed conductive gels or fluids in stretchable elastomers. Conductive media include liquid metals, hydrogels, ionogels, and organogels. Liquid metals include alloys, commonly eutectic gallium indium (EGaIn), that are liquids at room temperature[20]. Sensors utilizing 3D-printable EGaIn or EGaIn-based pastes have demonstrated effective performance at large strain ranges (≥100%)[21,22], but EGaIn is expensive and possesses uncertain biocompatibility[23]. Furthermore, the U.S. Department of Interior has designated indium along with rare-earth metals as a critical material[24], which highlights the poor sustainability of EGaIn-based sensors. Recently, there has been considerable interest in conductive hydrogels as a strain sensing medium due to their low cost, enormous strain ranges (up to 1000%), and tunable biomimetic properties[25]. While hydrogel systems can be very stable in aquatic environments, they are prone to instability due to

[1]Department of Materials Science & Engineering, University of Washington, Seattle, WA, USA. [2]Center for Research in Education and Simulation Technologies, University of Washington, Seattle, WA, USA. [3]Department of Surgery, University of Washington, Seattle, WA, USA. [4]Department of Mechanical Engineering, University of Washington, Seattle, WA, USA. ✉email: mcrump27@uw.edu

evaporation of water in air[25] and therefore have limitations for medical simulation applications. Ionogels, based on ionic liquids (ILs)[26,27], have been shown to be stable, low cost, high-strain, low-hysteresis sensing media when embedded in a stretchable elastomer[12,28]. However, the toxicity of many ionogels[29] has motivated the search for a similarly high-performance conductive gel with unequivocal biocompatibility[30].

The high cost of liquid metals, environmental instability of hydrogels, and toxicity of many ionogels have inspired the development of conductive organogels based on deep-eutectic solvents (DESs)[31,32]. DESs are liquid mixtures composed of a quaternary ammonium salt complexed with either a metal salt or a neutrally charged hydrogen bond donor (HBD)[31]; DESs possess a melting point lower than either constituent species. DESs and ILs share favorable physical properties, such as low vapor pressures, a wide liquid window, and limited flammability[33,34]. The inexpensive, nontoxic precursor feedstocks and facile, scalable synthesis of several DES compositions[31] make them an attractive alternative to ILs as an ionically conductive liquid utilized in strain sensors. The foreseeable risk of incidental dermal contact with the conductive channel during simulation exercises necessitates the selection of a nonhazardous medium.

In this work, inexpensive, conductive, and 3D-printable organogels utilizing a DES as the liquid medium and fumed silica particles as the gelating agent are introduced. The DES used in this work is composed of an HBD, polyethylene glycol (PEG200) or propylene glycol (PG), and the quaternary ammonium salt choline chloride (ChCl) in a 5 HBD: 1 ChCl molar ratio[35,36]. The HBDs PEG200 and PG were selected over the commonly used HBD ethylene glycol[37] due to their nontoxic nature and GRAS (generally recognized as safe) classifications by the U.S. Food and Drug Administration[38,39], and choline chloride is a biocompatible, mass-produced salt primarily used in animal feed[40]. In this work, we show that the surface functional group on the fumed silica particles drastically influences the DES/silica mixture rheology, and we report a class of shear-thinning organogels composed of a conductive DES and fumed silica particles with the functional group 3-trimethoxysilylpropylmethacrylate. Furthermore, we 3D-print stretchable strain sensor channels embedded in the elastomer polydimethylsiloxane (PDMS) with the PEG200-based organogel and silver-impregnated nylon thread serving as the conductive channel and electrode, respectively. Sensors achieve a large dynamic strain range (300%), negligible baseline drift, minimal hysteresis, and cyclic stability (1000 cycles at 100% strain amplitude). Finally, lifelike skin tissue models with monolithically integrated organogel strain sensors are fabricated and tested to showcase the potential applications in a dermatological surgical simulation.

RESULTS AND DISCUSSION

Sensorized Y/V plasty demonstration

A Y/V plasty (Fig. 1a) is a common, versatile technique in plastic surgery utilized to excise undesired tissue and minimize the formation of hypertrophic scars arising from cutaneous wounds, so Y/V plasty training is considered an important component of surgical education[41]. Therefore, a Y/V plasty suture training pad with monolithically integrated organogel strain sensors was developed (Fig. 1b and Supplementary Fig. 1). The pink- and yellow-colored PDMS layers represent the skin and fat layers, and the silicone recipes were selected to simulate a lifelike mechanical response and feel (Supplementary Fig. 2). A conductive organogel was 3D printed onto the PDMS skin layer (Fig. 1c) to serve as the strain sensing medium; conductive threaded electrodes were carefully inserted into every organogel channel and run to the edges of the pad to preserve the visual fidelity of the tissue model (Fig. 1d). A Y/V plasty suturing procedure was performed on a tissue model with monolithically integrated strain sensors (Fig. 1e and Supplementary Movie 1); the resistance of the strain sensor located in the flap was selected for measurement. The resistance of this sensor rapidly increased in response to the initial elongation experienced by the flap (Fig. 1e, insets i. and ii.). As more sutures were stitched, the resistance of the sensor remained constant (Fig. 1e, insets iii. and iv.). This was indicative of a successful suturing procedure as loosening sutures would result in retraction of the flap and a corresponding decrease in resistance.

Organogel synthesis and characterization

Fumed silica particles with different surface capping groups (Fig. 2a–c) were studied due to their efficacy as gelating agents in conductive ionogels[28]. A summary of the properties and FTIR spectroscopy results of the fumed silica particles investigated in this study can be found in Supplementary Table 1 and Supplementary Fig. 3, respectively. Per viscosity flow curve measurements (Fig. 2d), the addition of 4 or 8 wt.% R711 (3-trimethoxysilylmethacrylate-capped) fumed silica particles to the PEG-based DES converted the DES from a Newtonian fluid to shear-thinning fluids. Increasing the concentration of R711 to 12 wt.% resulted in a shear-thinning gel, a rheological quality necessary for effective 3D-printable inks[42]. The gel does not flow during the inversion test (Fig. 2d, inset), a result indicative of gelation. The presence of a linear viscoelastic region up to 0.1% strain followed by the crossover of the storage modulus (G') and the loss modulus (G'') as shear strain is increased further corroborates the formation and subsequent destruction of a gel structure, respectively (Fig. 2e). This rheological phenomenon has been observed for mixtures of a PEG400 (MW = 400 g/mol), and silica nanoparticles capped with 3-trimethoxysilylmethacrylate[43] or (3-glycidyloxypropyl)trimethoxysilane[44]. Shear-thinning, DES-based organogels utilizing cellulose nanostructures[45–47] or starch[48] as the thickening agent have been reported in literature, but shear-thinning DES-based organogels with fumed silica particles as the thickening agent have not been published. In contrast, viscosity curves for the samples containing R974 (methyl-capped) or 200 (hydroxyl-capped) fumed silica particles resulted primarily in shear-thickening fluids, or STFs (Fig. 2f, g). This rheological phenomenon is typical of many silica particle-glycol formulations[49]. As flow increases, these fumed silica particles tend to aggregate in non-equilibrium aggregates known as hydroclusters[50]. These shear-thickening fluids are typical of hydroxyl-capped fumed silica particles mixed with PEG[51,52]. With regards to R974, the incomplete coverage of the methyl capping group allows for hydrogen bonding between residual surface hydroxyl groups (~50%) on R974 and PEG that drive hydrocluster formation[53]. Viscosity flow curve measurements of PEG200 and fumed silica mixtures without ChCl revealed that the inclusion of ChCl increases the viscosity of the mixtures without affecting the predominant qualitative rheological trends (Supplementary Fig. 4). Similar rheological trends were reported for mixtures composed of several lithium salts in PEG300 and fumed silica particles capped with various surface functional groups[51,53]. Additionally, similar rheological behavior was observed for mixtures consisting of a PG-based DES and fumed silica particles (Supplementary Fig. 5), which showcases the compositional tunability of this class of conductive organogels. As the vapor pressure of PEG200 (1.69×10^{-2} Pa)[54] is three orders of magnitude lower than that of PG (18.9 Pa)[55] and the onset decomposition temperature of the PEG-based organogel was suitably high at 227.4 °C (Supplementary Fig. 6), the PEG-based organogel was selected as the conductive medium in the stretchable strain sensors reported here.

Freestanding sensor fabrication and characterization

Pairs of silver/nylon conductive composite electrodes were stitched ~15 mm apart into the PDMS substrate containing a

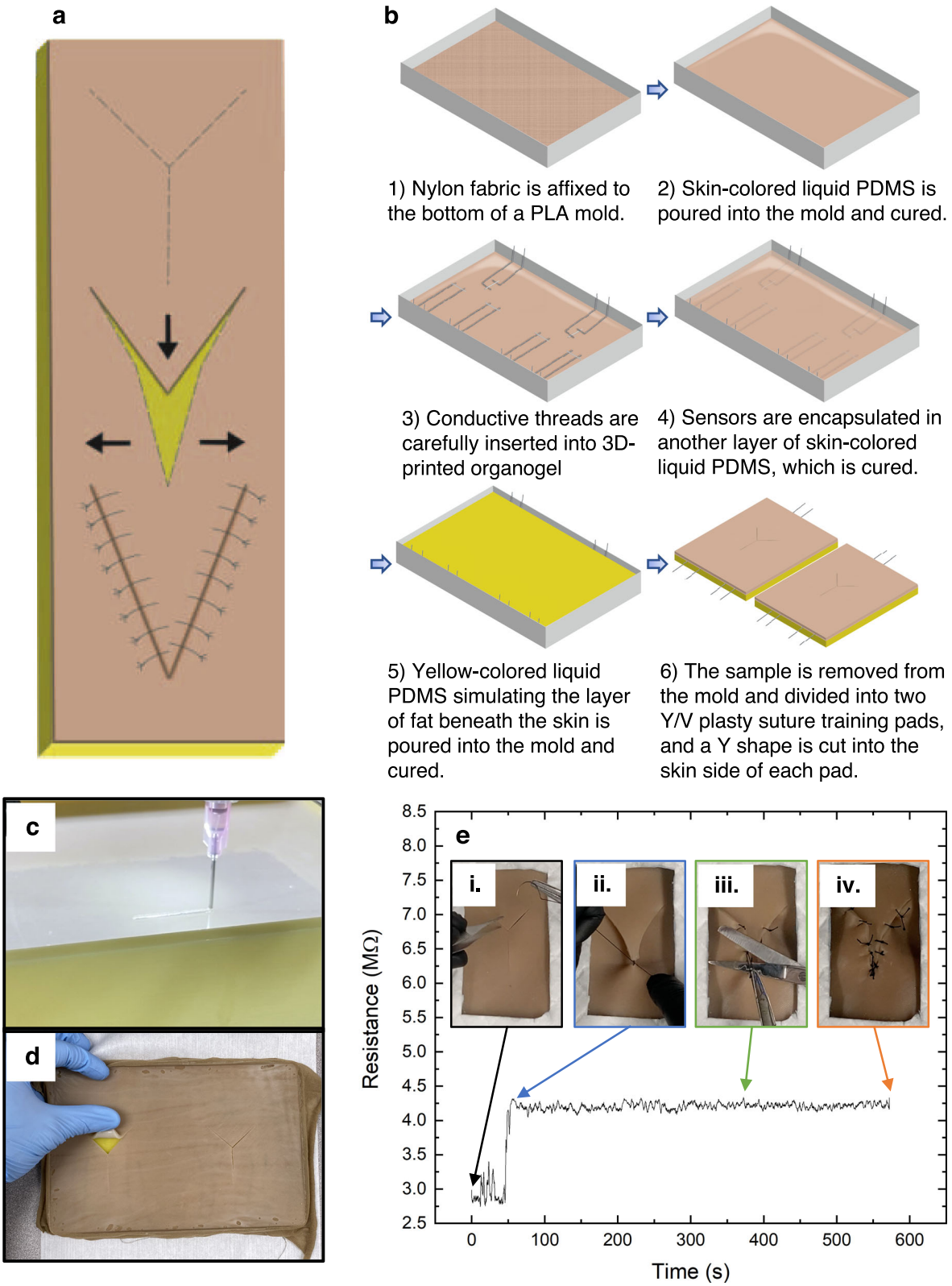

Fig. 1 Fabrication and demonstration of a sensorized Y/V plasty tissue model. In a Y/V plasty, a Y-shaped incision with the vertex located at the site of unwanted tissue is cut into the dermal layer, and the flap in the skin layer is pulled down and sutured into a V shape after excision (**a**). A sensorized Y/V plasty tissue suturing pad (**b**) is fabricated by encapsulating a conductive organogel and conductive thread electrodes within the skin layer of the pad. This organogel is 3D-printable (**c**) and visually imperceptible in the skin layer of the pad (**d**). The strain sensor located in the skin flap demonstrated a clear response to the elongation experienced by the flap during suturing (**e**).

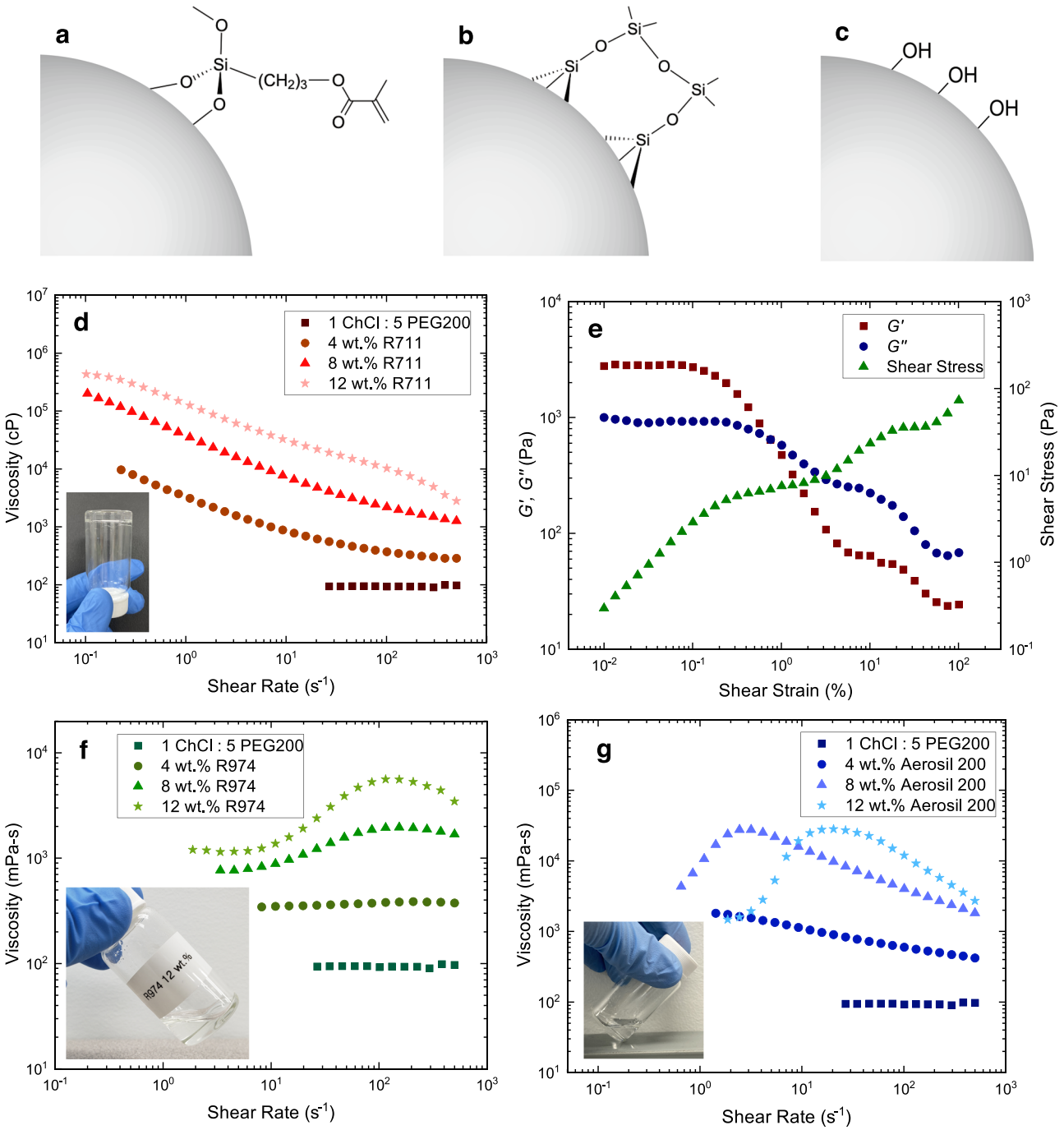

Fig. 2 Rheology of fumed silica/DES mixtures. Different surface capping groups are present on Aerosil R711 (3-trimethoxysilylmethacrylate-capped), R974 (methyl-capped), and 200 (hydroxyl-capped) fumed silica particles, respectively (**a**–**c**). Viscosity measurements (**d**) and the inversion test (**d**, inset) revealed that the mixture formed a shear-thinning gel when 12 wt.% of the trimethoxysilylmethacrylate-coated fumed silica (R711) was added to the PEG-based deep-eutectic solvent. An oscillatory amplitude sweep (**e**) performed on this mixture further indicated gel formation. In contrast, mixtures that used methyl-capped fumed silica (R974) consisted of shear-thickening fluids (**f**) when silica concentration was increased to 12 wt.%. A picture of the shear-thickening fluid with 12 wt.% R974 is shown in the inset of **f**. Mixtures that used hydroxyl-capped fumed silica (Aerosil 200) consisted of shear-thinning fluids at 4 wt.% and shear-thickening fluids at 8 and 12 wt.% (**g**). A picture of the shear-thickening fluid with 12 wt.% Aerosil 200 is shown in the inset of **g**.

sheet of nylon (Supplementary Fig. 7). This sheet of nylon serves as mechanical support for both these electrodes and for stitches performed in a dermatological simulation. Next, 25 mm lines of organogel were dispensed on the PDMS substrates using the 3D printer. The extra length ensured a complete connection between pairs of stitched electrodes. After printing, deposition of the subsequent PDMS layer encapsulated the printed lines (Supplementary Fig. 8) and plugged all holes made by the stitched electrodes. Sensors were cut into 64 ×10 mm rectangular samples for electromechanical characterization. Figure 3 indicated consistent, drift-free performance by the sensors. Dynamic ramp tests up to 200% strain (Fig. 3a and Supplementary Fig. 9a) and up to 300% strain (Fig. 3b and Supplementary Fig. 9b) show a monotonic response with a consistent return to the baseline

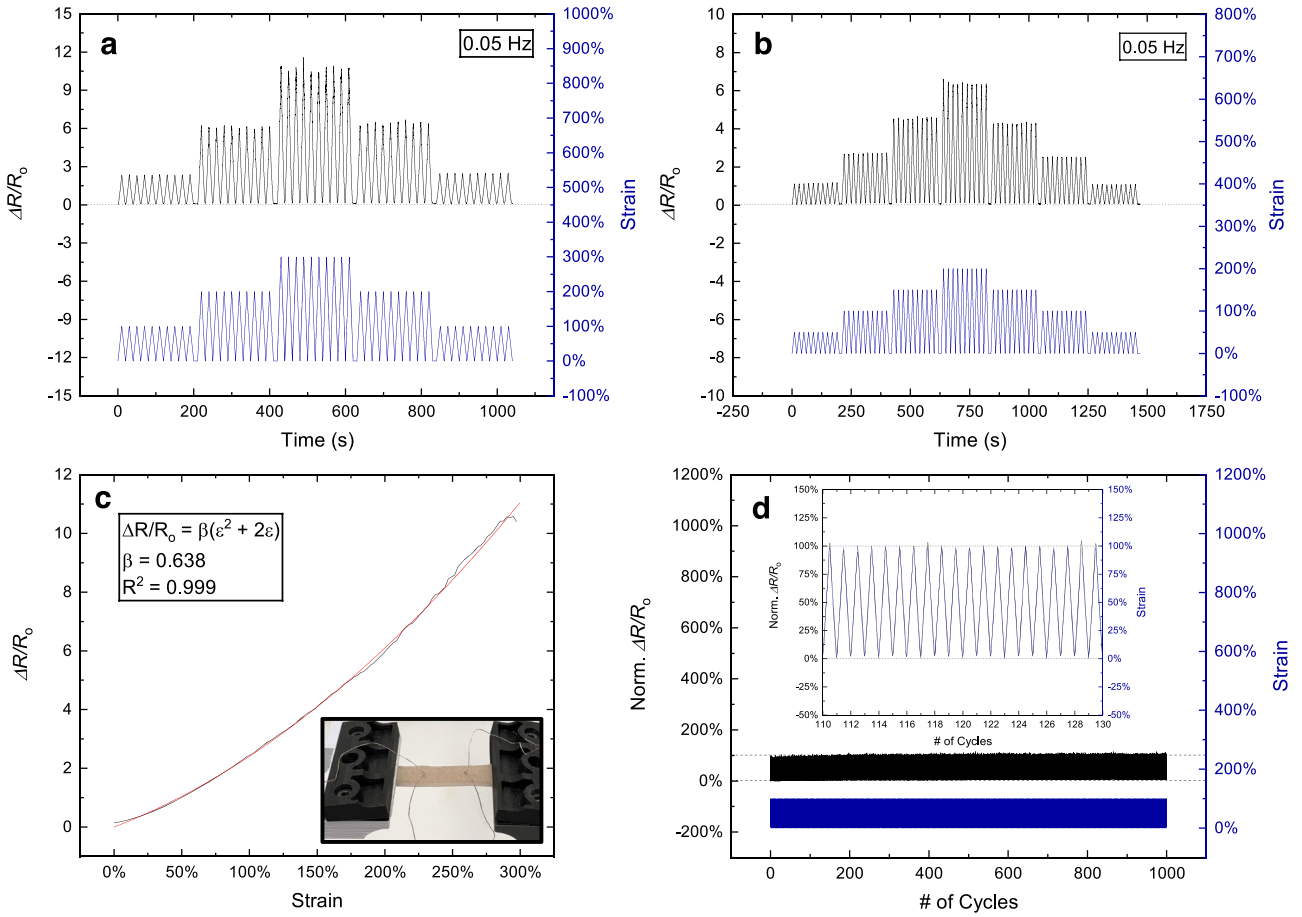

Fig. 3 Electromechanical characterization of strain sensors. Dynamic testing results (**a** and **b**) demonstrated a consistent electrical response up to 300% strain and no baseline drift for a frequency of 0.05 Hz. Horizontal dashed lines have been added to emphasize the lack of signal drift. An example of an extracted ramp test from a (**c**) revealed a parabolic relationship between the relative change in resistance and strain up to 300% strain. A picture of a strain sensor clamped in the electromechanical testing grips is shown in the inset of c. Cyclic testing up to 100% strain and 0.3 Hz resulted in minimal drift up to 1000 cycles (**d**), and normalized relative resistance results indicated excellent tracking of the amplitude and frequency of sensor actuation (**d**, inset).

resistance value for all ten cycles at varying amplitudes and frequencies. Furthermore, exposure to large strains do not distort the amplitudes of subsequent smaller strains. This reliable electromechanical response enables simplified sensor readout analysis compared to that required for composite-based sensors that demonstrate a nonmonotonic response[17–19]. As the strain failure limit of viscus[56] and dermal[57] tissue falls below 300% strain[58], the 300% strain amplitude achieved by these sensors endow them with integrability in a wide range of realistic tissue models. Ramp tests and hysteresis analysis extracted from the 20 peaks with a strain amplitude of 300%. The ramp tests (Fig. 3c and Supplementary Fig. 10) show a strong parabolic relationship between the relative change in resistance and strain ($R^2_{avg} = 0.998 \pm 0.001$, $n = 20$). The fitting parameter, β, reflects the contact resistance (R_c) of a strain sensor with a cylindrical sensing channel[59,60]:

$$\beta = \frac{(R_o - 2R_c)}{R_o} \quad (1)$$

where R_o represents the initial resistance of the sensor. A larger β value ($0 \le \beta \le 1$) indicates a lower contact resistance. The average β value of 0.621 ± 0.059 taken from the twenty peaks with a 300% strain amplitude (Fig. 3b and Supplementary Fig. 9b) is predictably lower than those of fluidic sensors that use wire electrodes (0.746–0.797[60,61]) due to the inferior conductivity of composite electrodes, but effective sensing is still realized, demonstrating the electromechanical robustness of the composite thread electrodes in place of wires. The extracted hysteresis results (Supplementary Fig. 11) show a low average degree of hysteresis of $1.34 \pm 0.76\%$ ($n = 20$), a value superior to those reported in fluid-based sensors using wires as electrodes over a similar strain range[12,60–64]. The compliance and porosity of composite thread electrodes enables improved adhesion between the electrodes and PDMS to reduce the degree of hysteresis. Cyclic testing (Fig. 3f) revealed a stable, drift-free performance of sensors stretched to 100% strain at 0.3 Hz for 1000 cycles, and the actuation amplitude and frequency tracked flawlessly (Fig. 3f, inset), indicating excellent reproducibility of these sensors. In comparison, 3D-printed deep-eutectic-solvent sensors recently reported by Lai et al. show significant baseline drift after 100 cycles of 30% dynamic strain[47]. Long-term stability measurements of twelve sensors stored in a desiccator revealed stable resistance readings up to one week after fabrication (Supplementary Fig. S12).

We introduce a class of shear-thinning organogels, which combine fumed silica particles with a deep-eutectic solvent comprised of choline chloride and biofriendly glycols. In addition, we report a stretchable strain sensor using this 3D-printable and inexpensive organogel as the sensing medium and conductive composite threads as the electrodes. Finally, we introduce a Y/V plasty suture training pad with monolithically integrated organogel strain sensors; the small sensor footprint preserves the fidelity of the simulation. The lack of drift, achievable strain amplitudes of

300% strain, and simple, monotonic response of these sensors suggests widespread applicability of this sensing technology to the quantification of soft tissue deformation in medical simulation. Reliable quantification of tissue deformation can generate real time, objective feedback for surgical rehearsal and medical education. We expect sensorized tissue models such as the additively manufactured one reported here to improve practitioner skill and confidence, leading to lower medical error rates. Future studies will focus on the development of organogel compositions with improved stability. Also, future work will focus on the development of simulation modules that require simultaneous multi-sensor detection of strain, as recent studies have reported such capabilities using piezoresistive ionogel-based soft sensors[28,65]. In addition, future work will include validation studies of the Y–V model with surgical trainees and also will expand on applications and capabilities using this 3D-printable gel. As the surface of the fumed silica utilized to induce a shear-thinning rheology is capped with the UV-sensitive 3-trimethoxysilylpropyl-methacrylate, UV-enabled technologies, such as sensors using 3D-printed auxetic frameworks[66] or UV-curable supercapacitors[67], will be explored.

METHODS

Organogel synthesis and characterization

Choline chloride (≥98%), propylene glycol (PG), and poly(ethylene glycol) with a molecular weight of 200 g/mol (PEG200) were purchased from Sigma–Aldrich, while all Aerosil® fumed silica particles (R711, R974, and 200) were provided gratis by Evonik. Fumed silica particles were characterized with FTIR spectroscopy in attenuated total reflectance mode (Thermo Scientific Nicolet iS10). Choline chloride was dried under vacuum at 130 °C for 72 h and stored in a nitrogen glovebox. A deep-eutectic solvent with a 1:5 molar ratio of choline chloride to PG or PEG200 was prepared and stirred for 2 h at 90 °C. Fumed silica particles were added to the deep-eutectic solvent with varying concentrations and mixed via a planetary mixer (Thinky ARV-310) at 2000 RPM for 10 min. The resulting gels and fluids were characterized by a rheometer (Anton Parr MCR302) at 20 °C using 25 mm parallel plates with a set height of 0.5 mm. Viscosity flow curves were taken over a shear rate domain of 0.1–500 s^{-1}. Oscillatory amplitude sweeps were carried out over a strain domain of 0.01–100% and a fixed frequency of 1 rad s^{-1}. Approximately 76.6 mg of organogel was weighed for thermogravimetric analysis (Mettler-Toledo TGA/DSC 3 +). The mass loss of the sample was measured under nitrogen from 27 to 720 °C with a heating rate of 5 °C min^{-1}.

Sensor fabrication

Nylon fabric (L'eggs) was placed in the bottom of a 130 × 200 mm 3D-printed PLA mold. Twenty grams of PlatSil® Gel-25 Part B silicone (Polytek) was added to a mixture of 20 g Gel-25 Part A and 20 g PlatSil® Deadener LV (Polytek). This was manually mixed for two minutes then poured into the mold and stippled into the taut nylon with a brush. The synthetic skin silicone layer was allowed to cure fully, ~30 min. Pairs of silver/nylon composite conductive threads (Agsis-Lite, Syscom Advanced Materials) were stitched into the substrates ~15 cm apart.

The PEG-based organogel was transferred to a syringe, and the syringe was centrifuged at 9000 RPM for 10 min to remove any trapped air bubbles. The syringe was then attached to the pneumatic SmartPump® on a 3D microdispenser (N-Scrypt 3Dn-300) attached to a two-axis translation stage. The silicone substrate was placed on the print chuck, and lines of organogel were dispensed onto it through a nozzle (blunt-tip needle, 20 G). 25 mm long lines were printed using a pressure of 35 psi, speed of 3 mm s^{-1}, and clearance of 0.6 mm. The sensors were then encapsulated by another layer of silicone composed of equimass amounts of Gel-25 A, Gel-25 B, and Deadener LV and allowed to cure at room temperature overnight.

Y/V plasty suture training pad fabrication

Similar to the sensor fabrication, a 60 g Gel-25 skin formulation colored with 0.5 g of Silc Pig™ Flesh pigment was poured over a taut nylon layer in the same printed mold. Each mold fits two Y/V Plasty training pads. Two sets of three 20 mm organogel lines were printed on the fully cured skin layer substrate. Conductive thread electrodes were placed 5 mm into the ends of each organogel line. The sensors were then embedded by another 60 g skin layer. After curing, a thin layer of petrolatum (Vaseline) was painted onto the middle of the skin layer; a 1-cm-thick petrolatum-free perimeter was established. An 80 g PDMS fat layer of 1:1:2 Gel-25 A:Gel-25 B:Deadener LV colored with 1 g of Silc Pig™ Yellow was poured into the mold. After 30 min, the suture training pad could be removed from the mold. A Y shape was cut into the skin layer by a scalpel and guided by a stencil (Supplementary Fig. 1). The size and shape of the Y cut was determined with input from two surgeons. Each line segment of the Y extends 30 mm from the nexus. Two sensors are perpendicular to the stem of the Y, 10 mm from the cut and 15 mm from the bottom of the Y. The third sensor is collinear with the stem and 27.7 mm above the Y junction.

Independent skin and fat layers were fabricated identically for mechanical characterization. Samples were cut into dog bone shapes using an ASTM D638 Type V cutting die.

Electromechanical characterization

Rectangular sensor samples (10 × 64 mm) were cut from the sheet. Sensors were clamped into custom 3D-printed, sandpaper lined grips on a dynamic mechanical tester (Electroforce Testbench, TA, USA). The sensors were preloaded to 0.1 N and the cross-sectional area was measured by laser micrometers (IG-028, Keyence Corp., Japan). The distance between thread electrode tips was taken as the gage length and was measured with calipers. Alternating square waves with an amplitude of ±2 V and a frequency of 50 Hz were applied by an impedance analyzer (VersaSTAT 3, Ametek, USA), and the resulting current was measured at a sampling rate of 500 Hz. The impedance analyzer was used to measure the electrical resistance of the third sensor located above the Y junction in the Y/V plasty demonstration.

The sensors first underwent a dynamic cyclic test with ten cycles at 0.05 Hz to 50, 100, 150, 200, 150, 100, and 50% strain, for a total of 70 cycles. This was immediately followed by a ramp to failure at 1% strain per second. Resistance vs. time results were consolidated by taking the mean resistance value of a combined negative and positive pulse (total duration of 0.04 s), and the results were synchronized manually to extrapolated strain vs. time results recorded from the dynamic mechanical tester. All results were smoothed with a 20-point adjacent-averaging smoothing routine.

The mechanical properties of independent skin and fat layers were characterized with a uniaxial tensile test performed at two different strain rates: 0.16 mm/s (quasistatic) and 3.0 mm/s (dynamic). Samples were strained either to failure or the maximum range of the dynamic mechanical tester (150 mm). The fat layer results were smoothed with a 5-point adjacent-averaging smoothing routine.

Sensor fabrication for sensor stability study

A clear skin layer was prepared, and 12 25-mm-long PEG-based organogel lines were dispensed using a 3D printer as described in Section 4.2. Then, conductive thread electrodes were placed directly into each line as described in Section 4.3. Then, the sensors were encapsulated using a clear skin layer of PDMS as described previously. The resistance of one sensor was continuously measured at 100 Hz with an LCR meter (LCR-600, Global Specialties) during the entire encapsulation process (Supplementary Movie 2), and the first ten minutes and last 5 seconds of the 60-minute encapsulation process were recorded with a video camera (iPhone 11 Pro, Apple).

DATA AVAILABILITY

The experimental data referenced to in this manuscript are available upon request to the corresponding author, M.R.C.

Received: 21 October 2020; Accepted: 16 February 2021;
Published online: 17 March 2021

REFERENCES

1. Grenvik, A. & Schaefer, J. From Resusci-Anne to Sim-Man: the evolution of simulators in medicine. *Crit. Care Med.* **32**, S56–S57 (2004).
2. Makary, M. A. & Daniel, M. Medical error—the third leading cause of death in the US. *BMJ* **353**, i2139 (2016).

3. Seam, N., Lee, A. J., Vennero, M. & Emlet, L. Simulation training in the ICU. *Chest*. **156**, 1223–1233 (2019).
4. Sachdeva, A. K. Educational interventions aimed at the transition from surgical training to surgical practice. *Am. J. Surg.* **217**, 406–409 (2019).
5. McGaghie, W. C., Issenberg, S. B., Cohen, M. E. R., Barsuk, J. H. & Wayne, D. B. Does simulation-based medical education with deliberate practice yield better results than traditional clinical education? A meta-analytic comparative review of the evidence. *Acad. Med. J. Assoc. Am. Med. Coll.* **86**, 706 (2011).
6. Beal, M. D. et al. The effectiveness of medical simulation in teaching medical students critical care medicine: a systematic review and meta-analysis. *Simul. Health.* **12**, 104–116 (2017).
7. Noureldin, Y. A., Lee, J. Y., McDougall, E. M. & Sweet, R. M. Competency-based training and simulation: making a "valid" argument. *J. Endourol.* **32**, 84–93 (2018).
8. Harn, H. I. et al. The tension biology of wound healing. *Exp. Dermatol.* **28**, 464–471 (2019).
9. Dai, J., Bordeaux, J. S., Miller, C. J. & Sobanko, J. F. Assessing surgical training and deliberate practice methods in dermatology residency: a survey of dermatology program directors. *Dermatol. Surg.* **42**, 977–984 (2016).
10. Sajan, J. A. et al. Validated assessment tools for reconstructing facial defects in simulation. *Otolaryngol. Neck Surg.* **149**, P44–P45 (2013).
11. Amjadi, M., Kyung, K. U., Park, I. & Sitti, M. Stretchable, skin-mountable, and wearable strain sensors and their potential applications: a review. *Adv. Funct. Mater.* **26**, 1678–1698 (2016).
12. Crump, M. R. et al. Monolithic 3D-printing of embeddable and highly stretchable strain sensors using conductive ionogels. *Nanotechnology* **30**, 364002 (2019).
13. Yamada, T. et al. A stretchable carbon nanotube strain sensor for human-motion detection. *Nat. Nanotechnol.* **6**, 296 (2011).
14. Lim, H. et al. Advanced soft materials, sensor integrations, and applications of wearable flexible hybrid electronics in healthcare, energy, and environment. *Adv. Mater.* **32**, 1901924 (2020).
15. Sekitani, T. et al. A rubberlike stretchable active matrix using elastic conductors. *Science* **321**, 1468–1472 (2008).
16. Truby, R. L. & Lewis, J. A. Printing soft matter in three dimensions. *Nature* **540**, 371 (2016).
17. Zheng, Y. et al. High-performance wearable strain sensor based on graphene/cotton fabric with high durability and low detection limit. *ACS Appl. Mater. Interfaces* **12**, 1474–1485 (2019).
18. Zhao, M. et al. A multifunctional and highly stretchable electronic device based on silver nanowire/wrap yarn composite for a wearable strain sensor and heater. *J. Mater. Chem. C.* **7**, 13468–13476 (2019).
19. Zhou, C.-G. et al. Highly stretchable and sensitive strain sensor with porous segregated conductive network. *ACS Appl. Mater. Interfaces* **11**, 37094–37102 (2019).
20. Daeneke, T. et al. Liquid metals: fundamentals and applications in chemistry. *Chem. Soc. Rev.* **47**, 4073–4111 (2018).
21. Votzke, C. & Daalkhaijav, U. Highly-stretchable biomechanical strain sensor using printed liquid metal paste. in *IEEE Biomedical Circuits and Systems Conference (BioCAS)* (2018).
22. Malakooti, M. H., Bockstaller, M. R., Matyjaszewski, K. & Majidi, C. Liquid metal nanocomposites. *Nanoscale Adv.* **2**, 2668–2677 (2020).
23. Kim, J.-H., Kim, S., So, J.-H., Kim, K. & Koo, H.-J. Cytotoxicity of Gallium–Indium liquid metal in an aqueous environment. *ACS Appl. Mater. Interfaces* **10**, 17448–17454 (2018).
24. Ellis, L. U. S. Department of the Interior—Office of the Secretary: Final List of Critical Minerals 2018. *Fed. Regist.* **83**, 23295–23296 (2018).
25. Wang, Z., Cong, Y. & Fu, J. Stretchable and tough conductive hydrogels for flexible pressure and strain sensors. *J. Mater. Chem. B* **8**, 3437–3459 (2020).
26. Marr, P. C. & Marr, A. C. Ionic liquid gel materials: applications in green and sustainable chemistry. *Green. Chem.* **18**, 105–128 (2016).
27. Le Bideau, J., Viau, L. & Vioux, A. Ionogels, ionic liquid based hybrid materials. *Chem. Soc. Rev.* **40**, 907–925 (2011).
28. Truby, R. L. et al. Soft somatosensitive actuators via embedded 3D printing. *Adv. Mater.* **30**, 1706383 (2018).
29. Costa, S. P. F., Azevedo, A. M. O., Pinto, P. C. A. G. & Saraiva, M. L. M. F. S. Environmental impact of ionic liquids: recent advances in (eco) toxicology and (bio) degradability. *ChemSusChem* **10**, 2321–2347 (2017).
30. Gomes, J. M., Silva, S. S. & Reis, R. L. Biocompatible ionic liquids: fundamental behaviours and applications. *Chem. Soc. Rev.* **48**, 4317–4335 (2019).
31. Smith, E. L., Abbott, A. P. & Ryder, K. S. Deep eutectic solvents (DESs) and their applications. *Chem. Rev.* **114**, 11060–11082 (2014).
32. Paiva, A. et al. Natural deep eutectic solvents–solvents for the 21st century. *ACS Sustain. Chem. Eng.* **2**, 1063–1071 (2014).
33. Wu, S.-H., Caparanga, A. R., Leron, R. B. & Li, M.-H. Vapor pressure of aqueous choline chloride-based deep eutectic solvents (ethaline, glyceline, maline and reline) at 30–70 C. *Thermochim. Acta* **544**, 1–5 (2012).
34. Shahbaz, K. et al. Thermogravimetric measurement of deep eutectic solvents vapor pressure. *J. Mol. Liq.* **222**, 61–66 (2016).
35. Kuehn, K. M., Massmann, C. M. & Sovell, N. R. Choline chloride eutectics: low temperature applications. *J. Undergrad. Res.* **15**, 5 (2017).
36. Troter, D. Z. et al. Choline chloride-based deep eutectic solvents in CaO-catalyzed ethanolysis of expired sunflower oil. *J. Mol. Liq.* **266**, 557–567 (2018).
37. Ibrahim, R. K. et al. Physical properties of ethylene glycol-based deep eutectic solvents. *J. Mol. Liq.* **276**, 794–800 (2019).
38. LaKind, J. S., McKenna, E. A., Hubner, R. P. & Tardiff, R. G. A review of the comparative mammalian toxicity of ethylene glycol and propylene glycol. *Crit. Rev. Toxicol.* **29**, 331–365 (1999).
39. Zhou, T., Xiao, X., Li, G. & Cai, Z. Study of polyethylene glycol as a green solvent in the microwave-assisted extraction of flavone and coumarin compounds from medicinal plants. *J. Chromatogr. A* **1218**, 3608–3615 (2011).
40. Frauenkron, M., Aktiengesellschaft, B., RUIDER, G. Ü. N. & HO, H. Ethanolamines and propanolamines. *Environ. Prot.* **421**, 8 (2012).
41. Khalil, P. N., Siebeck, M., Mutschler, W. & Kanz, K. G. The use of chicken legs for teaching wound closure skills. *Eur. J. Med. Res.* **14**, 459 (2009).
42. Highley, C. B., Rodell, C. B. & Burdick, J. A. Direct 3D printing of shear-thinning hydrogels into self-healing hydrogels. *Adv. Mater.* **27**, 5075–5079 (2015).
43. Yu, M., Qiao, X., Dong, X. & Sun, K. Effect of particle modification on the shear thickening behaviors of the suspensions of silica nanoparticles in PEG. *Colloid Polym. Sci.* **296**, 1767–1776 (2018).
44. Pattanayek, S. K. & Ghosh, A. K. Dynamic shear rheology of colloidal suspensions of surface-modified silica nanoparticles in PEG. *J. Nanopart. Res.* **20**, 53 (2018).
45. Sirviö, J. A. Cationization of lignocellulosic fibers with betaine in deep eutectic solvent: Facile route to charge stabilized cellulose and wood nanofibers. *Carbohydr. Polym.* **198**, 34–40 (2018).
46. Selkälä, T., Sirviö, J. A., Lorite, G. S. & Liimatainen, H. Anionically stabilized cellulose nanofibrils through succinylation pretreatment in urea–lithium chloride deep eutectic solvent. *ChemSusChem* **9**, 3074–3083 (2016).
47. Lai, C.-W. & Yu, S.-S. 3D printable strain sensors from deep eutectic solvents and cellulose nanocrystals. *ACS Appl. Mater. Interfaces* **12**, 34235–34244 (2020).
48. Selvanathan, V., Azzahari, A. D., Halim, A. A. A. & Yahya, R. Ternary natural deep eutectic solvent (NADES) infused phthaloyl starch as cost efficient quasi-solid gel polymer electrolyte. *Carbohydr. Polym.* **167**, 210–218 (2017).
49. Gürgen, S., Kuşhan, M. C. & Li, W. Shear thickening fluids in protective applications: a review. *Prog. Polym. Sci.* **75**, 48–72 (2017).
50. Liu, X.-Q. et al. Temperature induced gelation transition of a fumed silica/PEG shear thickening fluid. *Rsc Adv.* **5**, 18367–18374 (2015).
51. Raghavan, S. R., Walls, H. J. & Khan, S. A. Rheology of silica dispersions in organic liquids: new evidence for solvation forces dictated by hydrogen bonding. *Langmuir* **16**, 7920–7930 (2000).
52. Warren, J. et al. Effect of temperature on the shear-thickening behavior of fumed silica suspensions. *ACS Appl. Mater. Interfaces* **7**, 18650–18661 (2015).
53. Raghavan, S. R., Riley, M. W., Fedkiw, P. S. & Khan, S. A. Composite polymer electrolytes based on poly (ethylene glycol) and hydrophobic fumed silica: dynamic rheology and microstructure. *Chem. Mater.* **10**, 244–251 (1998).
54. Krieger, U. K. et al. A reference data set for validating vapor pressure measurement techniques: homologous series of polyethylene glycols. *Atmos. Meas. Tech.* **11**, 49–63 (2018).
55. Verevkin, S. P., Emel'yanenko, V. N. & Nell, G. 1, 2-Propanediol. Comprehensive experimental and theoretical study. *J. Chem. Thermodyn.* **41**, 1125–1131 (2009).
56. Kemper, A. R., Santago, A. C., Stitzel, J. D., Sparks, J. L. & Duma, S. M. Biomechanical response of human spleen in tensile loading. *J. Biomech.* **45**, 348–355 (2012).
57. Ottenio, M., Tran, D., Ní Annaidh, A., Gilchrist, M. D. & Bruyère, K. Strain rate and anisotropy effects on the tensile failure characteristics of human skin. *J. Mech. Behav. Biomed. Mater.* **41**, 241–250 (2015).
58. Joodaki, H. & Panzer, M. B. Skin mechanical properties and modeling: a review. *Proc. Inst. Mech. Eng. Part H. J. Eng. Med.* **232**, 323–343 (2018).
59. Matsuzaki, R. & Tabayashi, K. Highly stretchable, global, and distributed local strain sensing line using GaInSn electrodes for wearable electronics. *Adv. Funct. Mater.* **25**, 3806–3813 (2015).
60. Choi, D. Y. et al. Highly stretchable, hysteresis-free ionic liquid-based strain sensor for precise human motion monitoring. *ACS Appl. Mater. Interfaces* **9**, 1770–1780 (2017).
61. Chen, G. et al. Superelastic EGaIn composite fiber sustaining 500% tensile strain with superior electrical conductivity for wearable electronics. *ACS Appl. Mater. Interfaces* **12**, 6112–6118 (2020).
62. Liu, C., Han, S., Xu, H., Wu, J. & Liu, C. Multifunctional highly sensitive multiscale stretchable strain sensor based on a graphene/glycerol–KCl synergistic conductive network. *ACS Appl. Mater. Interfaces* **10**, 31716–31724 (2018).
63. Yoon, S. G., Park, B. J. & Chang, S. T. Highly sensitive microfluidic strain sensors with low hysteresis using a binary mixture of ionic liquid and ethylene glycol. *Sens. Actuators A Phys.* **254**, 1–8 (2017).

64. Wu, Y. et al. Liquid metal fiber composed of a tubular channel as a high-performance strain sensor. *J. Mater. Chem. C.* **5**, 12483–12491 (2017).
65. Truby, R. L., Katzschmann, R. K., Lewis, J. A. & Rus, D. Soft robotic fingers with embedded Ionogel sensors and discrete actuation modes for somatosensitive manipulation. in *2019 2nd IEEE International Conference on Soft Robotics (RoboSoft)* 322–329 (IEEE, 2019).
66. Wong, J. et al. 3D printing Ionogel auxetic frameworks for stretchable sensors. *Adv. Mater. Technol.* **4**, 1900452 (2019).
67. Qin, H. & Panzer, M. J. Chemically cross-linked poly (2-hydroxyethyl methacrylate)-supported deep eutectic solvent gel electrolytes for eco-friendly supercapacitors. *ChemElectroChem* **4**, 2556–2562 (2017).

ACKNOWLEDGEMENTS

We would like to thank the Clean Energy Institute (CEI), the Washington Clean Energy Testbeds (WCET), the Washington Research Foundation, the state of Washington, the Center for Research in Education and Simulation Technologies (CREST), the U.S. Department of Defense (#W911NF-16-2-0147), and Jack Norfleet of the U.S. Army Research Laboratory for their support. We would also like to thank Hazel Williams of CREST for her contributions to the development of the Y/V plasty suture pad recipe and Dr. Lauren Poniatowski for performing the Y/V suturing depicted in Fig. 1.

AUTHOR CONTRIBUTIONS

All authors contributed to the preparation of this manuscript. M.C., S.B., F.P., R.S., and D.M. conceived the original ideas presented in this work. M.C., R.S., and D.M. supervised the overall project. S.B. and A.G. developed the Y/V suture pad. M.C. and S. B. developed the fabrication of the freestanding sensor and 3D printing of the organogel. M.C., F.P., and S.B. performed rheological and material characterization. M. C., S.B., and A.G. carried out electromechanical characterization of the Y/V plasty and freestanding sensors. F.P. provided technical guidance on 3D printing.

COMPETING INTERESTS

The authors declare no competing interests.

ADDITIONAL INFORMATION

Supplementary information The online version contains supplementary material available at https://doi.org/10.1038/s41528-021-00104-0.

Correspondence and requests for materials should be addressed to M.R.C.

Reprints and permission information is available at http://www.nature.com/reprints

Publisher's note Springer Nature remains neutral with regard to jurisdictional claims in published maps and institutional affiliations.